Pergamon

PII: S0301-9322(96)00014-6

Int. J. Multiphase Flow Vol. 22, No. 5, pp. 863–881, 1996

0301-9322/96 $15.00 + 0.00

MEASUREMENTS OF THE PARTICLE–FLUID VELOCITY CORRELATION AND THE EXTRA DISSIPATION IN A ROUND JET

J. SAKAKIBARA[1], R. B. WICKER[2] and J. K. EATON[3]

[1]Department of Mechanical Engineering, Keio University, Japan
[2]Department of Mechanical Engineering, University of Texas, El Paso, U.S.A.
[3]Department of Mechanical Engineering, Stanford University, U.S.A.

(Received 1 August 1995; in revised form 18 February 1996)

Abstract—Measurements of the particle/fluid velocity correlation and the dissipation of turbulent kinetic energy by particles were made in the near field of an axisymmetric jet laden with either 55 or 86 μm diameter glass beads. A digital particle-image-velocimetry system was adapted to measure simultaneously the velocity of fine tracer particles and larger dispersed particles. The particle/fluid velocity correlation was measured directly using the simultaneous measurements and indirectly using separate phase-locked measurements in an acoustically-forced jet. The direct measurements produced correlation values which were too low and the indirect measurements were too high, so the two techniques bracketed the correlation. Surprisingly, the correlation increased with increasing particle time-constant because the mean velocity of the heavier particles was closer to the convection velocity of the vortex rings in the jet. The dissipation of fluid turbulent kinetic energy by the particles was calculated using the phase-locked velocity measurements along with phase-locked particle concentration measurements. The results showed that the extra dissipation is large near the jet centerline, but quite small in the shear layer where the production is large.

Key Words: particle/fluid velocity correlation, extra dissipation, round jet, particles, digital PIV

1. INTRODUCTION

Turbulent gas flows laden with fine particles are commonplace in technological devices ranging from chemical vapor deposition systems to pulverized-coal burners. We are interested in flows where the particle loading is small enough that inter-particle collisions are rare and the motion of an individual particle is determined by its interaction with the gas flow. Also, the overall flow features are weakly affected by the presence of the particles, although there may be significant changes to the turbulent motions. There are two main particle/fluid interactions that are important in such cases. First, transport of the particles by both the mean and fluctuating fluid motions produces dispersion of the particle concentration. An initially high particle concentration will spread out with an apparent diffusivity which is dependent on both the properties of the flow and the particles. The second important interaction is the so-called "back-effect" of particles on the flow. Particles have a larger inertia and thermal mass than an equivalent fluid point so they can enhance the transport of momentum and energy from one region of the flow to another. This can lead to significant attenuation of the turbulence when the particles are very fine (c.f. Kulick *et al.* 1994).†

An important goal of researchers examining particle-laden flows is to develop models for both particle dispersion by turbulence and turbulence attenuation by particles. It is difficult to obtain accurate data from experiments, and there are far too few data sets available to develop empirical correlations that could guide model development. Resorting to theory, we reach a major impasse: almost all of the theories require some knowledge of the fluid velocity in the neighborhood of particle. However, the path of the particle is not known *a priori* so development of an expression for the fluid velocity surrounding the particle is difficult. Consider the motion of a particle moving

†There is disagreement about what constitutes a "fine" particle in this regard. The particle may either have a diameter which is much smaller than some eddy length scale or it may have a Reynolds number which is below some threshold. The distinction is unimportant in the present context.

only under the influence of viscous drag in a statistically homogeneous flow. Such a particle is characterized by an aerodynamic time constant, τ_p that is a function of the particle size and density and the fluid properties. If τ_p is of the same order as the turbulence time scale, the particle will follow a fluctuating trajectory that deviates from the path of a fluid element. Calculation of the trajectory requires knowledge of the fluid velocity surrounding the particle. Of course, this velocity cannot be known without first knowing the trajectory.

A similar problem arises in analyzing the attenuation of turbulence by particles. An exact transport equation for the turbulent kinetic energy of the gas phase is:

$$\frac{Dk}{Dt} = \left.\frac{Dk}{Dt}\right|_{\text{singlephase}} - \frac{1}{\rho_f}\overline{u_i f_{Di}} \qquad [1]$$

where the first term on the right comprises the production, dissipation, and transport terms in the single phase equation, u_i is the fluid velocity, and f_{Di} is the drag force per unit volume exerted by the particles on the fluid in the ith direction. This equation applies as long as the volume fraction of the particles is negligible. The second term on the right is called the extra dissipation of turbulent kinetic energy due to particles, ϵ_p. This expression may be made more useful by assuming a linear drag law for the particles. In that case, ϵ_p can be written as:

$$\epsilon_p = \frac{\bar{C}}{\rho_f \tau_p}(\overline{u_i u_i} - \overline{u_i v_i}) + \frac{1}{\rho_f \tau_p}(\overline{c u_i u_i} - \overline{c u_i v_i}) + \frac{1}{\rho_f \tau_p}(\overline{U_i} - \overline{V_i})\overline{c u_i} \qquad [2]$$

where C and c are the mean and fluctuating particle concentration (mass/unit volume) and the v_i are the particle velocity components. Further assuming that the particle concentration is uncorrelated with the fluid velocity,† the extra dissipation can be written:

$$\epsilon_p = \frac{\bar{C}}{\rho_f \tau_p}[\overline{u_i u_i} - R_{fpi}(\overline{u_i'^2})^{1/2}(\overline{v_i'^2})^{1/2}] \qquad [3]$$

where R_{fpi} is the correlation coefficient between fluid and particle velocity fluctuations.

We see then that the correlation between particle and fluid velocity fluctuations is an important parameter in the modeling of particle-laden flows and our problem is in finding a way to measure the correlation. Since the particle occupies a finite volume and causes a local disturbance of the flow, we formally define R_{fpi} as the correlation between the particle velocity and the fluid velocity in a small neighborhood surrounding the particle. This definition and the equations above are not useful unless a small neighborhood can be found over which the velocity is uniform. Practically, this means that the particle must be significantly smaller than the smallest length scales of the turbulent velocity fluctuations and that we must measure the fluid velocity at several points surrounding the particle.

There have been several recent attempts to evaluate the fluid-particle velocity correlation. Kiger & Lasheras (1995) made phase-locked measurements of the velocity of polydisperse droplets in a forced mixing layer using a phase-Doppler velocimeter. The smallest droplets acted as flow tracers, allowing them to calculate the difference between the phase-averaged fluid and particle velocities. This will produce a reasonable estimate of the fluid/particle velocity correlation as long as almost all of the velocity fluctuations are captured in the phase-averaged measurements. This technique would not work in fully three-dimensional turbulence. Beckel *et al.* (1995) are using a combined experimental/simulation system in a fully-developed, two-dimensional channel flow. The fluid velocity is measured with a two-component LDV that is moved along the path of a simulated particle. The path is calculated in real time using the measured fluid velocity to infer the drag on the particle.

While both of the experiments mentioned above have provided important information on particle/fluid interaction, neither has provided a direct measurement of the particle/fluid velocity correlation. Hassan *et al.* (1992) developed a PIV technique capable of simultaneously measuring the velocity of tracer particles and individual bubbles. They applied the system to measurement

†This assumption holds in most cases for which turbulence attenuation is large, but in cases where the particle Stokes number is near one, there may be a strong correlation between the fluid velocity and particle concentration fields (see Eaton & Fessler 1994).

of the velocity field around 1 mm diameter bubbles rising slowly in mineral oil. Their technique required operator intervention in the evaluation of each velocity field, so it was not applicable to the present case where thousands of velocity fields were required. However, their work showed that two phases could be clearly discriminated in PIV images and that the velocities of both phases could be measured simultaneously.

The objectives of the present experiment were to develop a fully automated, digital particle image velocimetry (DPIV) system capable of simultaneously measuring the velocity of a particle and the surrounding fluid. Experiments were conducted in the near-field of a turbulent axisymmetric jet flow operated at a Reynolds number of 9300. The turbulence in such flows is dominated naturally by axisymmetric vortex rings as illustrated for example by figures 4 and 5 of Longmire & Eaton (1992). Three dimensional turbulent motions are also present, but the largest fraction of the turbulent velocity fluctuations are produced by the vortex rings. In a natural jet, the vortex rings have random size and spacing within certain narrow limits. However, many experiments have shown that weak sinusoidal pulsing of the jet using acoustic drivers produces a periodic train of vortex rings as illustrated in figure 7 of Longmire & Eaton. Three dimensional turbulent motions persist, but are dominated by the velocity fluctuations due to the vortex rings.

In the present case, we forced the jet to allow phase-locked measurements similar to those of Kiger & Lasheras (1995). In this technique, measurements are made at a specific position in the jet and at a specific phase of the sinusoidal forcing. The velocities of the fluid and particles are measured in separate experiments, but at identical conditions. The relative velocity between the particles and fluid is determined by subtracting the two sets of measurements. Statistical quantities are obtained by averaging over all phase angles (0–360°) of the forcing. This technique does not take into account any velocity fluctuations that are not correlated to the forced motion. We also made direct measurements of the relative velocity by measuring simultaneously the fluid and particle velocities. This latter technique does take into account all of the motions of the fluid, not just those correlated to the forced motion. The jet was forced in both cases so that we could directly compare the measurements made by the two techniques. In addition, the phase-locked velocity measurements were used along with phase-locked particle concentration measurements to compute the extra dissipation term in the turbulent kinetic energy transport equation.

This paper presents the development of the DPIV technique and the results for two particle sizes in the near field of a round jet. The results indicate that the technique is useful in fully three-dimensional flows where phase-locking is impossible.

2. EXPERIMENTAL APPARATUS AND TECHNIQUES

2.1. Experimental facility

The experiment was conducted in the near field of the coaxial air jet facility described by Wicker & Eaton (1994a). The apparatus (see figure 1) has a central axisymmetric jet of 20 mm diameter surrounded by a 60 mm diameter annular jet. The central jet was the primary flow of interest and was laden with both the dispersed phase particles and fine tracer particles. The annular jet was operated at a very low velocity ($\cong 0.2$ m/s) and served mainly to provide entrainment flow that was well seeded with tracer particles. This eliminated the need to seed the entire room with tracer particles.

Air from a central compressor was supplied through individually metered lines to the core flow and annular plena. The air was seeded with 1 μm diameter titanium dioxide tracer particles downstream of the flow meters. The core flow then passed to the feed pipe where particles were injected into the flow using an Accurate Model 302 screw feeder. The core flow then entered a 50 mm diameter plenum chamber exiting downward through a 6.45:1 area ratio nozzle with a 20 mm exit diameter. The annular plenum chamber had a cross-sectional area of 158 cm^2, and the annular flow discharged through a 6.30:1 area ratio nozzle with a 60 mm exit diameter. The core nozzle had a knife-edge exit boundary condition so the annular stream was 20 mm wide at the nozzle exit.

A Scan-Speak 18W/8541 165 mm diameter audio speaker was coupled to the upper end of the core flow plenum to provide periodic flow excitation. The excitation served to phase lock the vortex ring structures in the core jet shear layer. The driving waveform was generated by an IBM XT

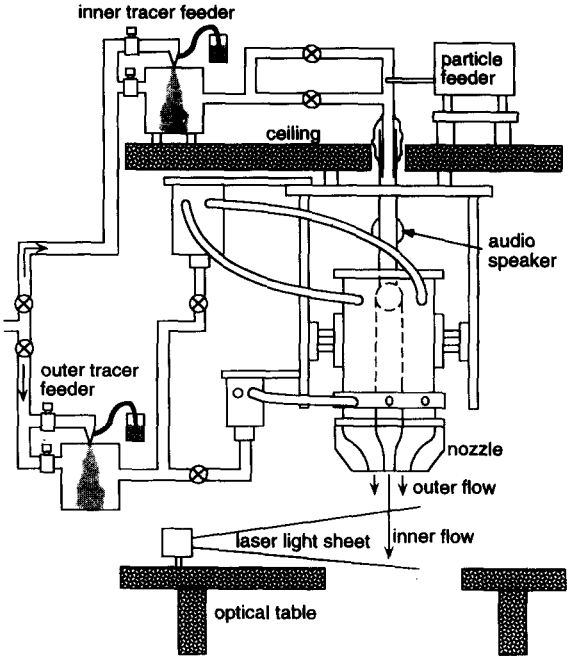

Figure 1. Sketch of the apparatus.

computer with a Data Translation DT2801 multifunction board. The computer-generated waveform was low-pass filtered and amplified before being supplied to the speaker. Single frequency, sine wave forcing was used for all the experiments reported here.

Two different sets of aerodynamically classified glass beads were used as the dispersed phase. Wicker & Eaton (1994b) measured the particle size distributions using a Coulter counter. The smaller particles had a number mean diameter of 55 μm and a standard deviation of 4.6 μm. The larger particles had a number mean diameter of 86 μm and a standard deviation of 12.5 μm. Typical aerodynamic time constants for the two sets of particles were 21 and 48 ms, respectively, for the smaller and larger particles.

2.2. Measurement system and procedure

The velocity of both the fluid tracer particles and the dispersed glass beads were measured using a custom Digital Particle Image Velocimetry (DPIV) system. The system components are illustrated in figure 2. The primary components were a double-pulsed laser sheet, a black and white video camera, and an 8-bit frame grabber mounted in an IBM-compatible 386 PC. To insure adequate spatial resolution of the DPIV measurements, only a short length of the jet was imaged at any one time.

The double-pulsed light sheet was formed by rapidly sweeping two laser beams through the measurement region. The beam from a Lexel 5W Argon-ion laser was split into two equal-strength beams using a cubic beam splitter and a mirror. The beams crossed each other on the surface of a rotating mirror spinning at 20 rev/s. The rotating mirror was driven by a brushless DC motor with closed loop speed control. Within the measurement region, the beams were separated by 14 mm and they crossed a given point 73 μs apart.

An area approximately 20 mm long in the axial direction by 30 mm in the radial direction was imaged onto a Sony XC-75 CCD camera. Two photo-transistors (PT1, PT2) were located in the laser sheet plane to provide synchronizing pulses to a timing control circuit. The camera timing was set so that the first laser sweep was captured on one video frame and the second sweep on the next frame. The timing circuit checked that the timing was correct and sent a signal to the computer that a valid image pair was available. The images were then captured using a Data Translation DT2867-LC frame grabber in the 386 PC. Finally, the two images were stored for later processing. The other lab computer supplying the forcing waveform also supplied a second voltage

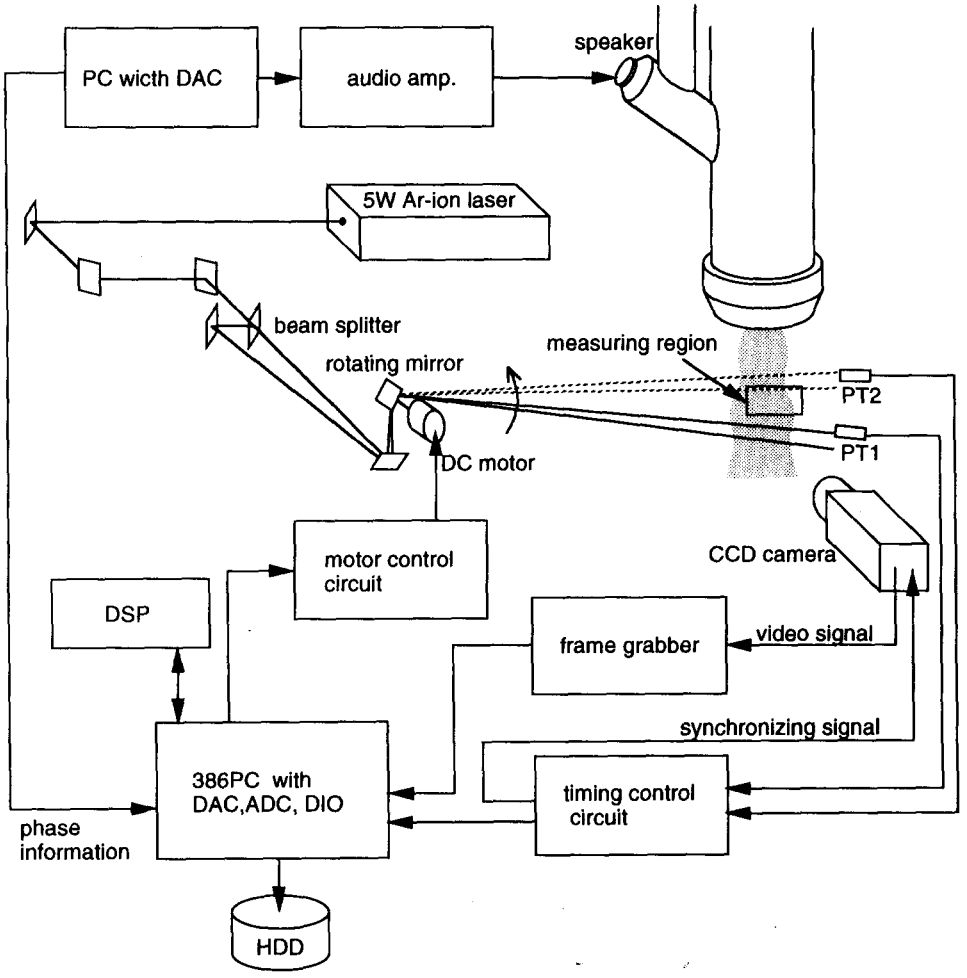

Figure 2. The DPIV system set up on the jet apparatus.

signal proportional to the phase of that waveform. This signal was recorded along with the image data to phase-tag the image pair. Typically, between 2000 and 4000 image pairs were captured and stored prior to processing.

The fluid velocity field was calculated from the stored images using the cross-correlation technique described in Sakakibara *et al.* (1993). For this processing, the image was divided into sub domains that contained 25 × 25 pixels corresponding to a spatial resolution of approximately 1 mm in the streamwise and radial directions. The spatial resolution in the out-of-plane direction was defined by the effective thickness of the laser sheet, which was approximately 1.5 mm. The measurement uncertainty of the instantaneous velocity data is determined by the resolution of the cross correlation. For the measurements reported here the uncertainty is ± 0.26 m/s. The statistical uncertainty in the averaged results is dependent on the number of samples. Typical statistical uncertainties are smaller than the measurement resolution except near the edge of the jet where relatively few particles were measured.

The difference between the present system and other DPIV systems was the addition of software for discrimination of the large particles from the small, flow-tracer particles. The large particles were typically 50–100 times larger in diameter than the tracer particles. Thus, the scattered light intensity was of the order of 1000 times greater for a large particle. The camera and lighting were adjusted so that even the largest tracer particles produced a pixel intensity of less than 70% of the maximum. With these settings, the scattered light from a large particle completely saturated a cluster of pixels and made the large particle appear to be 5–10 times larger than its actual size. The saturation and apparent increase in the particle size were used to locate large particles that were centered in the light sheet. The first pre-processing step was to set a threshold in the frame

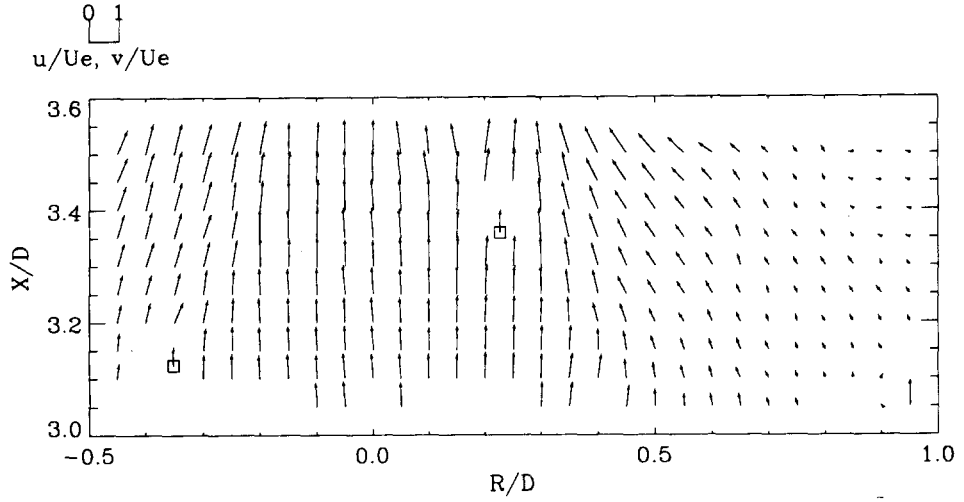

Figure 3. Instantaneous velocity field showing particle velocities as small squares with vectors and fluid velocity as plain vectors.

grabber so that any pixel values less than 70% of the maximum were set to zero. This eliminated the images of any tracer particles. A pattern matching algorithm was then used to find the center location and size of the large particles. The reference pattern was a Gaussian bump with a radius typical of the large particle images. The 1/e radius was 11 pixels for the 86 micron particles and nine pixels for the 55 micron particles. A cross-correlation between the reference pattern and the stored image was calculated and the peak locations of the cross-correlation were identified as the centers of large particles. Typically, between one and five large particles were captured in an image. The apparent size of a particle relates to the depth of the particle in the laser sheet; a particle in the center of the sheet appearing the largest. To obtain a rough measure of the apparent particle size, the images were compared to a set of five geometrically similar reference patterns each with a different size. Each reference pattern was centered on the particle and a cross correlation was calculated. The size of the particle was then said to be equal to the most correlated reference pattern. Particles with a small apparent size were eliminated since they were most likely at the edge of the light sheet, out of the main measurement plane. This allowed us to restrict the measurement plane thickness to approximately 2 mm. Finally, the particle velocity was obtained by cross correlation between the two successive video frames. The spatial resolution of the cross-correlation technique was 0.01 mm yielding an uncertainty in the particle velocity measurement of 0.19 m/s. As a final step in the processing, the fluid velocity data calculated in the first processing step were blanked out for the locations of the large particles.

Figure 3 shows a typical instantaneous velocity field. The square symbols with vectors indicate the position and velocity of the large particles. The remaining vectors indicate the fluid velocity. Note that only a few large particles are present in any instantaneous image. The measurements presented below will demonstrate the utility of the measurement technique. This same technique will probably work well for larger particles, but would not be expected to work for particles smaller than about 40 μm in diameter. Smaller diameter particles would be too difficult to discriminate from the flow tracer.

2.3. Phase averaging

The strong forcing produces a very periodic vortex ring structure that persists beyond the end of the potential core. Therefore, the velocity at any point in the jet near field is periodic in time except for small-scale turbulent fluctuations. The period of the velocity oscillation is the same as the period of the forcing waveform. We define a phase angle ϕ which varies from 0 to 360° during each cycle of the forcing waveform. At a given phase angle, a vortex ring will be located at a fixed position in the jet. It would be possible to acquire velocity measurements for different locations in the field all at the same phase. This would give a picture of the vortex as it would appear at

an instant in time. We instead chose to measure the velocity in a three mm long slice ($\Delta X/D = 0.15$) of the jet located at $X/D = 3.2$, measuring the velocity for all possible phase angles.

Many DPIV images were acquired each at a random time. The phase angle of the forcing waveform was recorded at the instant each image was acquired so that the phase average could be calculated. The phase average $\tilde{a}$, of any property a at particular phase angle ϕ and at the radial location r is

$$\tilde{a}(r, \phi_j) = \left\langle a(r) \Big|_{\phi_j - \frac{\Delta\phi}{2} \leq \phi < \phi_j + \frac{\Delta\phi}{2}} \right\rangle \quad [4]$$

where, $\langle\ \rangle$ denotes an ensemble average, and $\Delta\phi$ is width of the phase bins. Sixteen phase bins of width 22.5° were used.

We desire a spatial representation of the data which will show the fluid and particle velocities in the neighborhood of a vortex ring. The temporally phase-averaged flow can be converted to a spatial representation using Taylor's hypothesis with a measured convection velocity, U_c. The ith component of fluid velocity of the 'imaginary' flow field $\hat{u}_i$ is defined as

$$\hat{u}_i(r, x, t) \equiv \tilde{u}_i\left(-\frac{2\pi\{x + tU_c(r)\}}{\lambda}, r\right) \quad [5]$$

where λ is the vortex wavelength determined using the measured convection velocity and the known forcing frequency. The convection velocity of the vortex ring was evaluated by measuring the spatial correlation of the streamwise velocity as a function of streamwise spacing Δx. The correlation function is defined as:

$$R(\Delta t, \Delta x) = \frac{\int u_x(x, t) \cdot u_x(x + \Delta x, t + \Delta t)}{\sqrt{\int u_x(x, t)^2} \sqrt{\int u_x(x + \Delta x, t + \Delta t)^2}} \quad [6]$$

where the velocities are fluctuating quantities. The convection velocity was then evaluated from

$$U_c = \frac{\Delta x}{\Delta t_{R_{max}}} \quad [7]$$

where $\Delta t_{R_{max}}$ is Δt such that the R has maximum value. Figure 4 shows the radial distribution of the convection velocity at $X/D = 3.2$. It is nearly constant with a value of $U_c = 0.65\ U_e$.

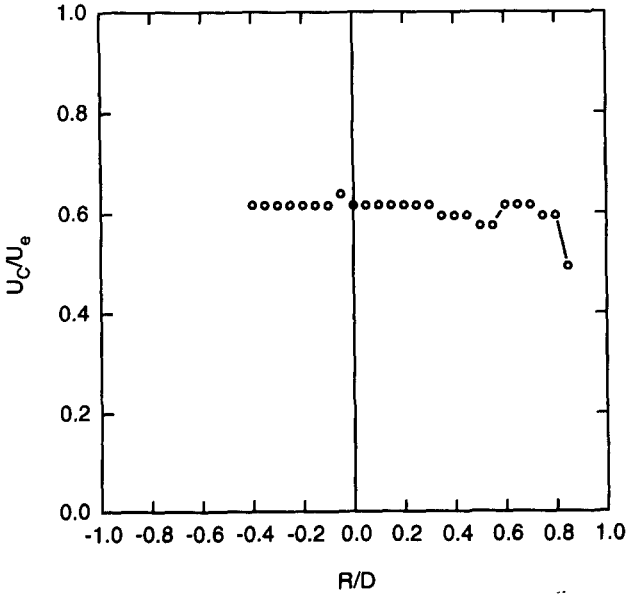

Figure 4. Vortex ring convection velocity as a function of radial position.

2.4. Flow conditions

The flow velocity at the jet exit was set at $U_e = 7.0$ m/s which corresponds to a Reynolds number $U_e D/v$ of 9.3×10^3. The centerline turbulence intensity measured at $X/D = 0.5$ was approximately 1% of the mean when the flow was unforced. The flow was forced at a frequency of 160 Hz corresponding to a Strouhal number (fD/U_e) of 0.46. At this frequency, the shear layer rolls up into a series of strong vortex rings, and no pairing is observed in the jet near field. A relatively high forcing amplitude of 4.8% was used to avoid phase jitter. The particle mass loading (m_p/m_{air}) was set to 0.0036. This insured that the particles did not affect the development of the flow. The light loading also avoided the occurrence of overlapping large particles in the images and prevented us from accidentally identifying out-of-plane large particles as fluid tracers. For each case, over 2000 video frame pairs were acquired and analyzed.

3. RESULTS AND DISCUSSION

3.1. Ensemble-averaged flow properties

Figure 5 shows the mean velocity profiles of the fluid and the two particle classes at $X/D = 0.5$. These profiles are shown as initial conditions for the downstream development of the jet. In this and all subsequent plots, the measurement region crosses the centerline of the jet, but only extends to the edge of the jet on the right-hand side. This limited measurement field was used in order to maintain the required spatial resolution. Radius values are labeled as negative on the left-hand side to avoid confusion. The fluid velocity profile is nearly a tophat at this location as expected with the well-contoured nozzle. The particle velocities are considerably lower than the fluid velocity because the particles cannot follow the rapid fluid acceleration in the nozzle. The 55 μm particles have a higher velocity than the 86 μm particles, but that velocity is still only about 65% of the fluid velocity.

Figure 6 shows mean streamwise velocity profiles for the fluid and particles at the primary measurement location, $X/D = 3.2$. The fluid velocity profile indicates that this location is very near the end of the potential core. The particle velocities are still lower than the fluid velocity for $R/D < 0.5$, and the 86 μm particles are moving more slowly than the 55 μm. Outside of the initial jet radius, the particles are moving faster than the fluid. This is because, particles that are flung out of the jet core retain their velocity due to their high inertia. This flattened particle velocity profile is typical of large particles in turbulent shear flows. Note that the 86 micron particles have a larger velocity than the 55 μm particles at the largest radius. There are no particle velocity

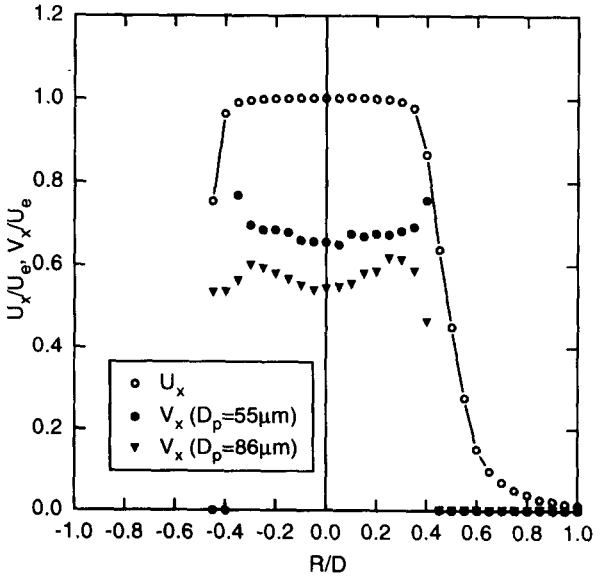

Figure 5. Mean velocity of the fluid and particles close to the jet exit ($X/D = 0.5$).

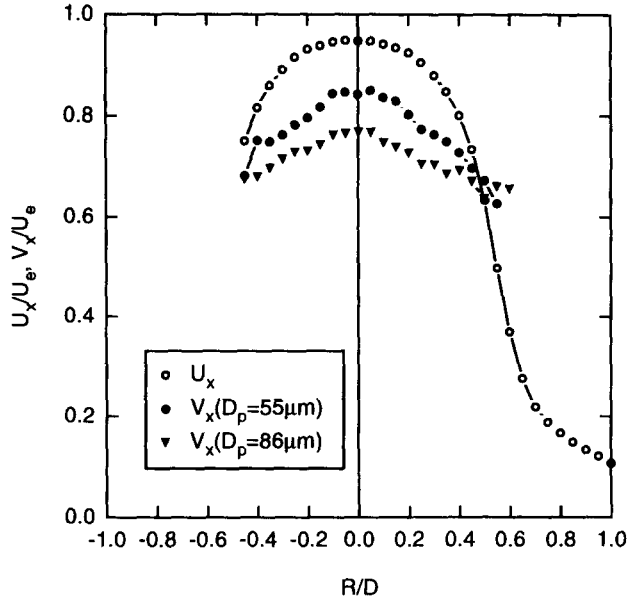

Figure 6. Mean axial velocity of the fluid and particles at $X/D = 3.2$.

measurements outside of $R/D = 0.6$ because the particle concentration was too low to obtain reliable statistics.

The radial mean velocity profiles are shown in figure 7. The fluid radial velocity is small and approximately antisymmetric as would be expected. The particle radial velocities are much larger because of the particle flinging by the vortex rings (Longmire & Eaton 1992). The radial particle velocity of the 86 μm particles is somewhat higher than that of the 55 μm particles.

Profiles of the standard deviation of the streamwise velocity of the fluid and particles are plotted in figure 8. The fluid rms profile has a strong peak at $R/D = 0.45$ and a weaker peak at $R/D = 0.65$. Such profiles are characteristic of strongly forced jets since the radial position of the vortex rings is effectively fixed. The standard deviation of the particle velocity is only about one half of the fluid

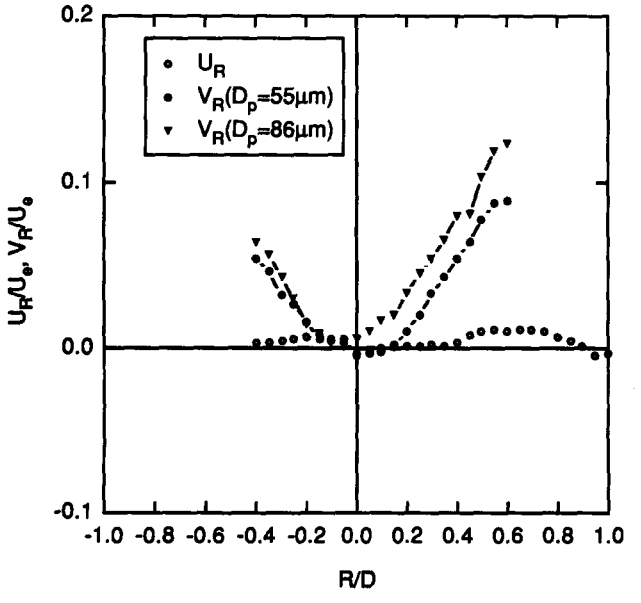

Figure 7. Mean radial velocity of the fluid and particles at $X/D = 3.2$.

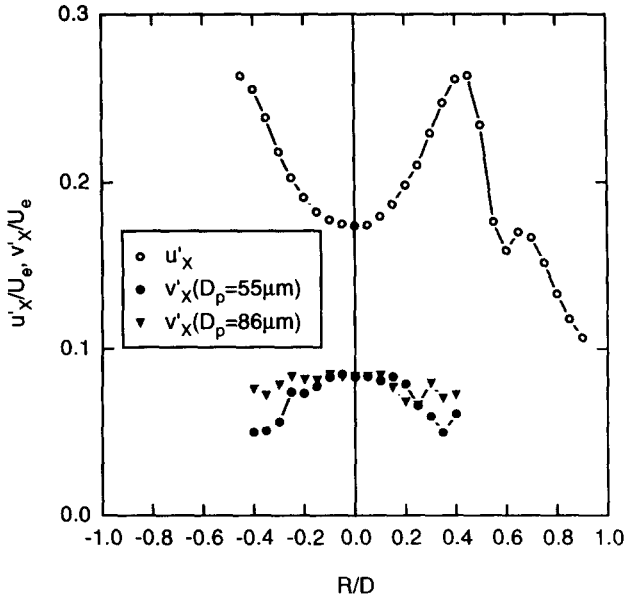

Figure 8. RMS axial velocity for the fluid and particles at $X/D = 3.2$.

rms at the center line. This is expected because of the poor response of the particles to the fluid motions. However, the fact that both particle sizes have the same rms velocity is somewhat surprising.

3.2. *Phase averaged flow properties*

The phase-averaged fluid velocity and particle concentration fields are plotted in figure 9(a) and (b) for the two particle sizes. The phase is incremented from right to left so the plot will resemble the spatial distribution that would be seen in an instantaneous image that is several jet diameters

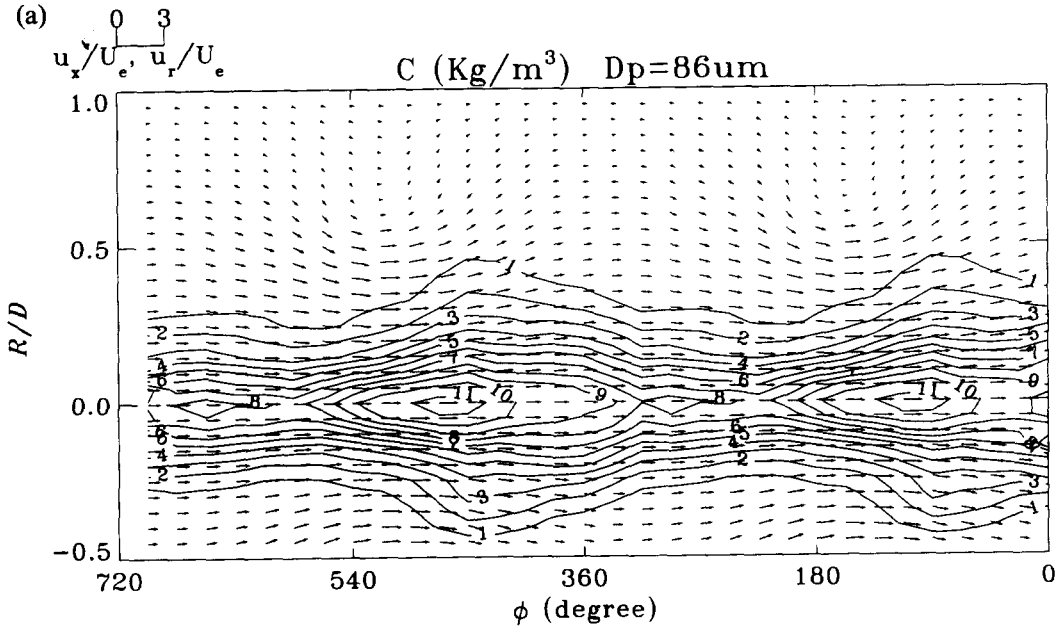

Figure 9. Phase averaged fluid velocity vectors and particle concentration contours for (a) 86 μm particles and (b) 55 μm particles. The concentration values are in kg/m^3 for an assumed mass loading ratio of unity.

[Fig. 9 continued opposite.]

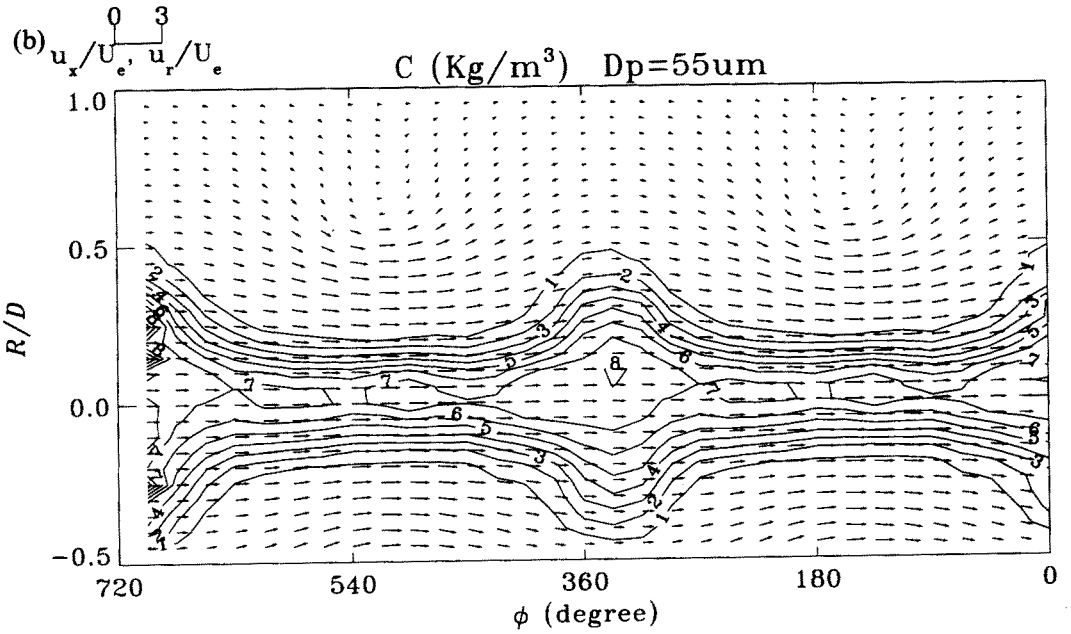

Fig. 9.

in length. Note that periodicity has been used to extend the domain in the phase direction. The fluid velocity vectors clearly show a ring vortex centered around $\phi = 180°$. The ring vortex produces a maximum in the streamwise velocity along the centerline at $\varphi = 180°$ and strong radial outflow around $\phi = 90°$.

The phase-averaged particle concentration distribution plotted as contours was measured by dividing the field into bins which were 22.5° long in the phase direction and 0.05 jet diameters wide in the radial direction. The measured values have been normalized so that the indicated average particle/fluid mass loading is unity. The plots show a cluster of high particle concentration formed along the centerline and particles flung radially outward forming a tongue protruding from the downstream side of the cluster. These patterns are very similar to those observed by Longmire

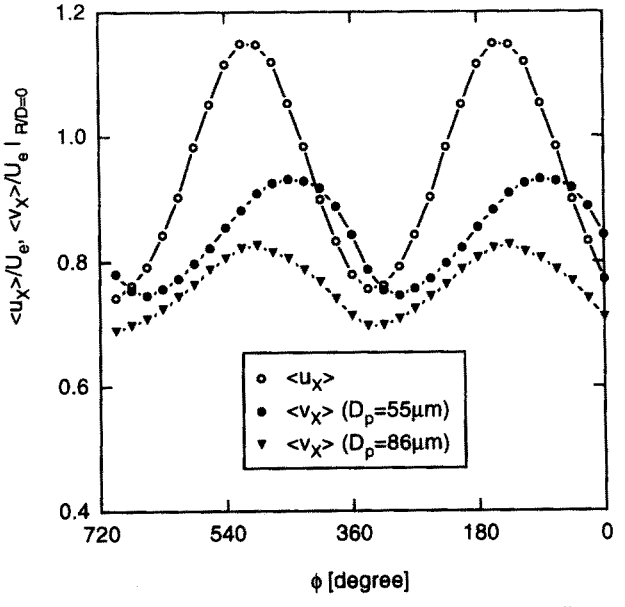

Figure 10. Phase-averaged axial velocity on the jet centerline.

& Eaton (1992) in a similar jet. The peak concentration is greater on the centerline for the larger particles while the radius of the tongues of particles extending out from the clusters is greater for the smaller particles. The Stokes number defined as the product of particle aerodynamic time constant and the forcing frequency was 3.4 and 7.7 for the 55 and 86 μm particles, respectively. The observed trends are identical to those found by Longmire & Eaton at these Stokes numbers. One interesting observation is that the peak concentration is located at different phases for the two particle sizes; $\phi = 120$ and 0° for the 86 and 55 μm particles, respectively. This is discussed further below.

Plots of the phase-averaged streamwise velocity for both the particles and the fluid on the jet center-line are shown in figure 10. The particle velocity fluctuations are significantly smaller than the fluid fluctuations as would be expected at this Stokes number. Also, the location of the peak particle velocity is phase-shifted relative to the fluid velocity. The 86 μm particles lead the fluid by approximately 15° and the 55 μm by approximately 60°. Also, the velocity waveform for the 55 μm particles is distorted relative to the nearly sinusoidal fluid velocity waveform. The phase shift is mainly caused by the difference between particle velocity and vortex ring convection velocity. Recall that the 55 μm particles were accelerated more quickly toward the jet velocity downstream of the jet exit. By $X/D = 3.2$, they have reached a velocity of approximately 0.85 U_e, 0.2 U_e greater than the convection velocity. The 86 μm particles have reached a velocity of 0.75 U_e considerably closer to the convection velocity. This difference also explains the difference in the location of the particle clusters.

3.3. *Measurement of the fluid/particle velocity correlation*

The fluid/particle velocity correlation, R_{fpi} was calculated from the velocity measurements using two different techniques. The first technique, called the indirect method, used the phase-averaged fluid and particle velocities to calculate the correlation coefficient as:

$$R_{fpi} = \frac{\int (\tilde{u}_i - U)(\tilde{v}_i - V)}{u_i' v_i'}$$

where u_i are fluid velocity components, v_i are particle velocity components, primed quantities are the rms values calculated from the phase-averaged data, capitalized quantities are the mean values, and the integral is taken over all phases of the forcing cycle. Note that this technique measures only the correlation of the coherent motions that are phase-locked to the forcing. Smaller-scale turbulence that is not phase-locked is also present in the flow. The particles probably cannot follow the higher frequency motions associated with this random turbulence. Thus, the true particle fluid correlation coefficient is probably lower than that measured by the indirect method.

The second, "direct" method uses the simultaneously measured fluid and particle velocity fields to calculate the correlation coefficient. Of course, the fluid velocity is not available at the precise location of the particle because the particle image covers an area significantly larger than the particle. We chose to use the fluid velocity measurements from the nearest position on either side of a large particle ($\Delta R/D = \pm 0.05$). Fluid velocity measurements from upstream and downstream of the particle were not used since they were affected by the local disturbance field around the particle. These direct measurements of the correlation coefficient are likely to produce values which are lower than the true measurement. Uncertainty (noise) in the measurement of the individual velocities is not likely to be correlated and will result in a lower measured correlation coefficient. This effect is largely eliminated by the phase-averaging of the indirect method.

Indirect measurements of the correlation coefficient for the streamwise velocity component are shown in figure 11. Near the jet center, the correlation is very high for both particle sizes, but especially so for the 86 μm particles. This is a very surprising result because we expect the correlation to be smaller for larger particles. However, the measurements can be explained by reference to figure 10. Recall that the 86 μm particles moved downstream at a velocity approximately equal to the vortex-ring convection velocity and that the fluid and particle velocity fluctuations were in phase. This results in a high correlation coefficient. The lighter 55 μm particles were moving approximately 0.2 U_e faster than the convection velocity. There was a substantial phase difference between the fluid and particle velocities resulting in the lower correlation coefficient. For both sizes

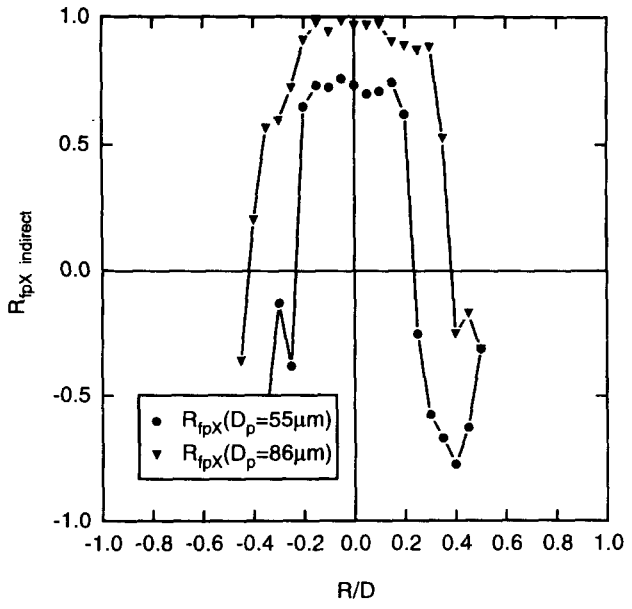

Figure 11. Indirect measurements of the particle/fluid axial velocity correlation, R_{fpx}.

of particles, the correlation becomes negative in the jet shear layer before oscillating around zero at large radii.

The direct measurements, plotted in figure 12, show substantially lower values of the correlation coefficient as expected. The trends are quite similar though with the 86 μm particles showing a broad plateau of nearly constant correlation coefficient while the correlation falls rapidly to negative values for the 55 μm particles. As argued above, the indirect measurements probably produce correlation coefficients which are too high while the direct measurements produce low values. For the 55 μm particles the two estimates are reasonably close near the jet center ($0.6 < R_{fpx} < 0.72$). For the 86 μm particles, the spread is wider ($0.6 < R_{fpx} < 0.98$), probably because the larger particles respond very poorly to the higher frequency motions in the flow. The rapid fall off of the correlation for the 55 μm particles in the shear layer is an artifact of the strong

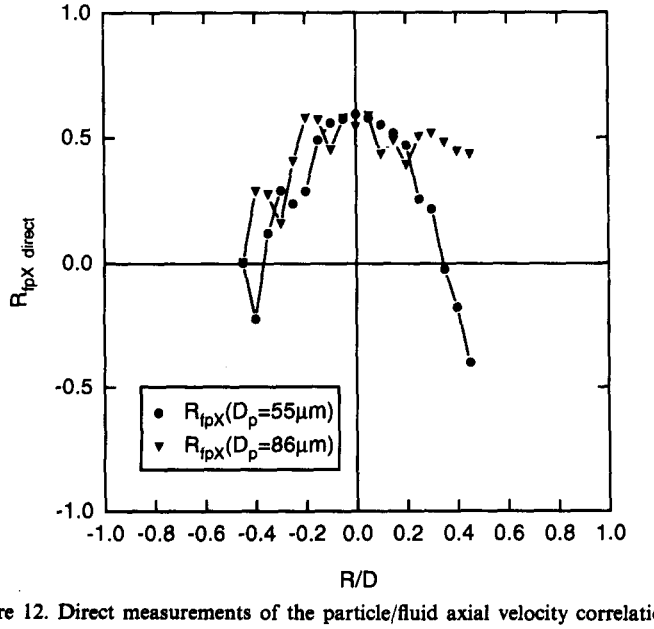

Figure 12. Direct measurements of the particle/fluid axial velocity correlation, R_{fpx}.

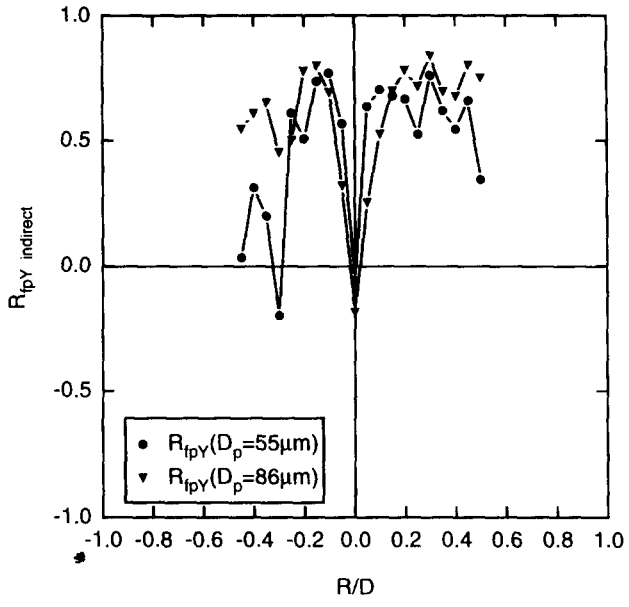

Figure 13. Indirect measurements of the particle/fluid radial velocity correlation, R_{fpr}.

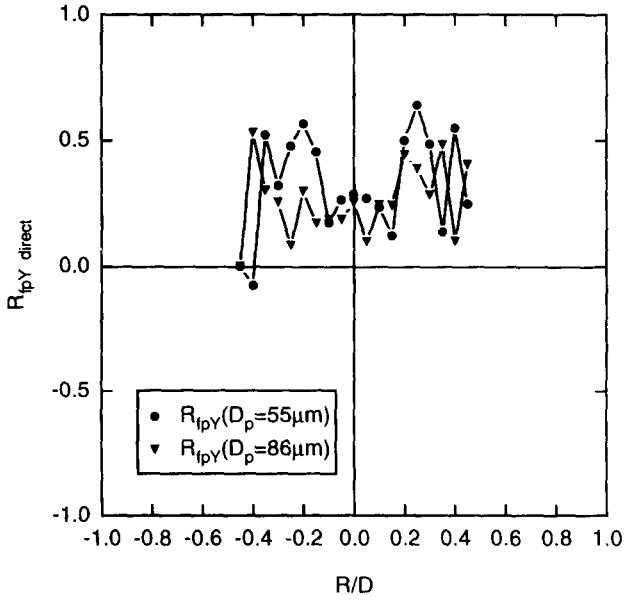

Figure 14. Direct measurements of the particle/fluid radial velocity correlation, R_{fpr}.

particle clustering found in this case. As seen in figure 9(b), there are very few particles outside of $R/D = 0.2$ for phase angles between 90 and 250°. The few particles measured in this range of phase angles are highly uncorrelated to the fluid velocity pulling down the overall average. These points will be of little consequence in evaluating the extra dissipation since the particle concentration is so small.

Plots of the radial component velocity correlation measured using the indirect and direct methods are shown in figures 13 and 14. The trends are similar to those shown above except the indirect measurements show zero correlation near the jet centerline.

3.4. Evaluation of the extra dissipation in the TKE equation

In this section we use the phase-averaged results presented in section 3.2 to calculate the extra dissipation due to particles. This is done for an assumed mass loading ratio (m_p/m_{air}) of one.

The actual mass loading was very small. We have thus implicitly assumed that a moderate loading of particles does not greatly affect the fluid velocity field. Longmire & Eaton (1992) did flow visualization experiments in a forced, axisymmetric jet at mass loadings up to about one. These experiments showed little qualitative change in the vortex structure. The results below can be scaled to smaller mass loadings, but extending them to higher mass loadings is probably not appropriate.

Equation [3] cannot be used to evaluate the extra dissipation term for the present case because of the strong correlation between the particle concentration and fluid velocity fields (see figure 9). One possibility is to use [2] to evaluate the extra dissipation term. However, in the present case, it is simplest to go back to the basic definition [1] and evaluate the instantaneous drag force as:

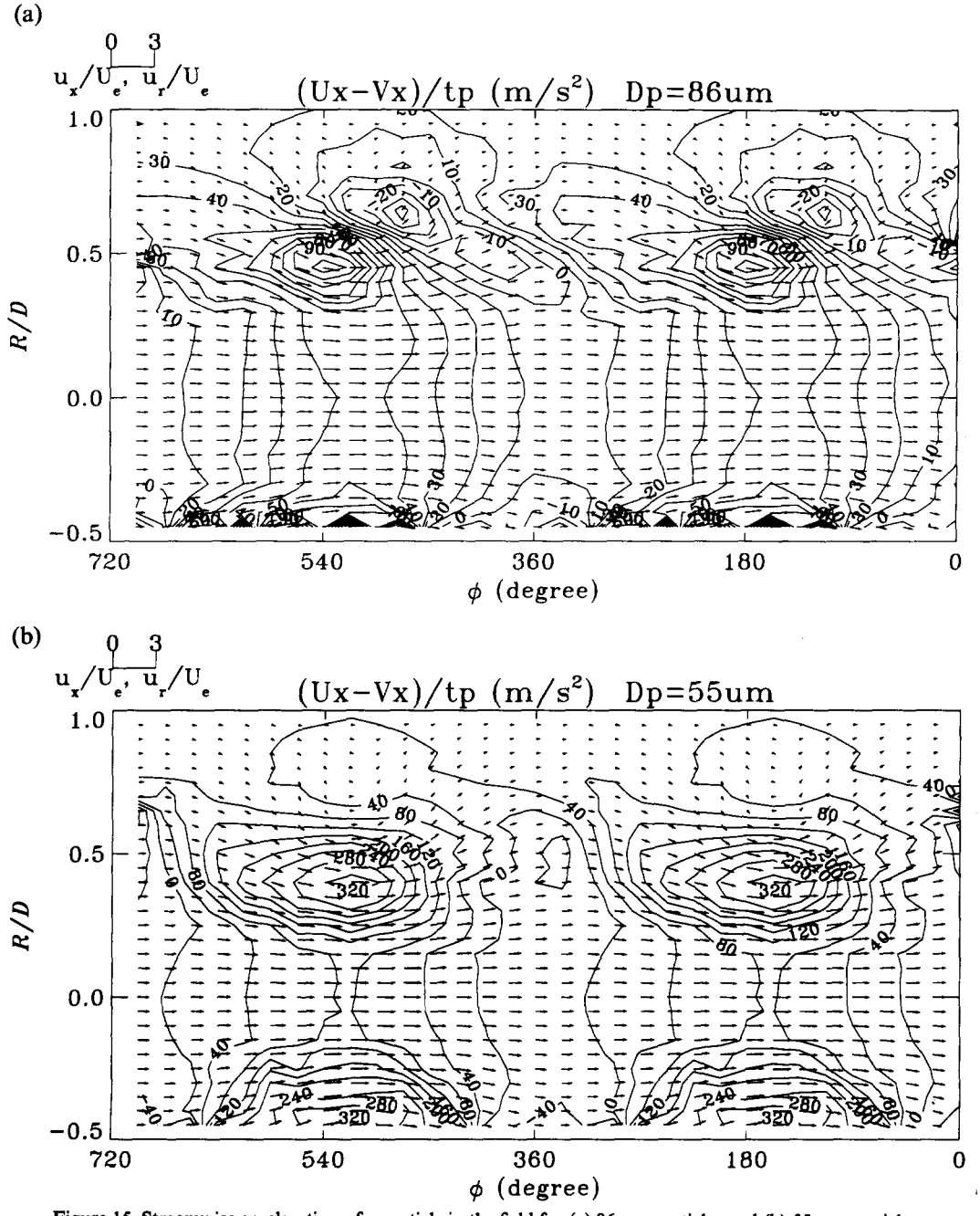

Figure 15. Streamwise acceleration of a particle in the field for (a) 86 μm particles and (b) 55 μm particles. The contour levels are in m/s^2.

$$f_{Di} = \frac{c(u_i - v_i)}{\tau_p} \qquad [10]$$

where the concentration and velocity components are taken to be instantaneous values. In practice, we use the phase-averaged quantities to compute the force in [10] then form the time average by averaging over all the phase angles.

Figure 15 shows the distribution of the quantity $(U_x - V_x)/\tau_p$. This is the streamwise acceleration of a single particle located anywhere in the field. This term is proportional to the drag on an individual particle. The highest acceleration for both particle sizes occurs near the core of the vortex rings ($\phi \sim 180°$) where the velocity difference between the fluid and particles is very large. This

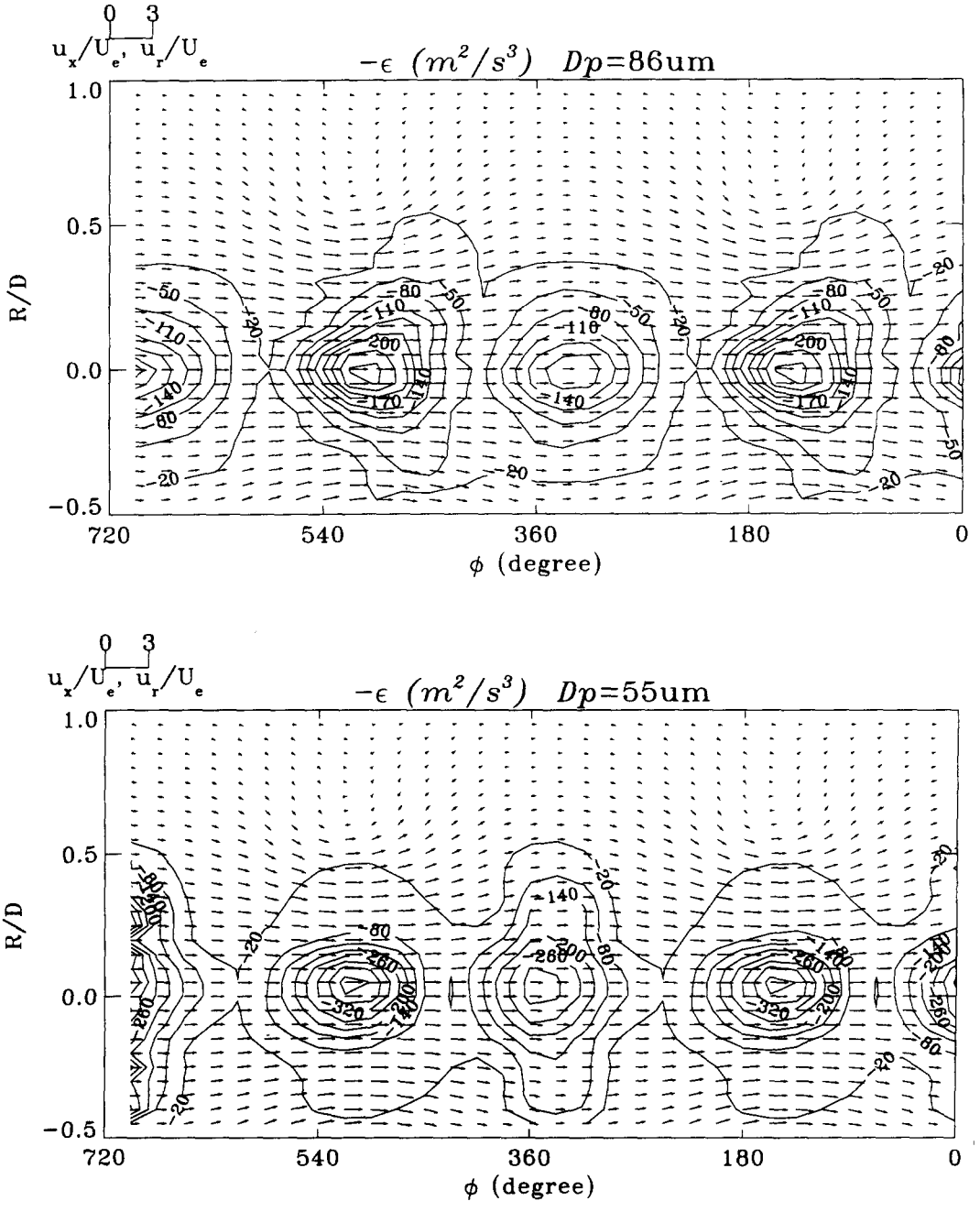

Figure 16. Fluid velocity vectors and the fluctuating particle drag force for an assumed mass loading ratio of unity; (a) 86 μm particles and (b) 55 μm particles.

is because the particles cannot follow the tightly curved streamlines in the vortex core region. As we will see below, these regions of high velocity difference are of little consequence because there are relatively few particles in the vortex cores. The minimum values occur near the jet centerline at $\phi \sim 360°$ where the fluid velocity reaches a minimum value approximately equal to the particle velocity. Negative values of the particle acceleration occur for the 55 μm particles where they are flung out by the vortex motion into a region of low fluid velocity.

The fluctuating streamwise drag force applied to a fluid element (f_{dx}) is calculated by multiplying $(U_x - V_x)/\tau_p$ by the phase averaged particle concentration C, and then subtracting the mean value. Here, the mean is calculated by averaging the calculated values at a given radius over all phases. The extrema of f_{dx} are located on the centerline where the particle concentration is greatest. The positive contours are elongated in the radial direction for the 55 μm particles near $\phi \sim 360°$ where the cluster of particles is located. The negative contours are radially elongated for the 86 μm particles near $\phi \sim 100°$. Once again, this corresponds to the location of the particle cluster for this case. The radial fluctuating drag force, f_{dr} was calculated in the same way and showed the same trends. The plots are omitted here for brevity.

The extra dissipation term was evaluated using the calculated values of f_{dx}, f_{dr} and the phase-averaged fluid velocity (minus the mean velocity). The results are shown in figure 16, plotted as a function of phase. The shapes of the contours are qualitatively the same as the contours of f_{dx}. However, the sign of ϵ_p is always positive, which means that particles act to dissipate the turbulence kinetic energy everywhere in the field. It must be noted that the contribution of the azimuthal component of the fluctuating drag to the extra dissipation has been ignored. However, this component is expected to be small relative to the axial and radial components in a flow dominated by nearly axisymmetric vortex rings. The largest values of the extra dissipation occur along the centerline with the strongest peak occurring in the middle of the vortex rings and a secondary peak midway between successive rings. This conclusion holds for both size particles even though the particle cluster is located in a different location for the two cases.

Usually the extra dissipation term is time averaged as indicated in [1]. In this case, we averaged over the phases (0–360°) at fixed radius to form an equivalent time average. The results are plotted in figure 17 for an assumed mass-loading ratio of 1.0. The fluid turbulence kinetic energy production is shown for comparison. As seen above, the extra dissipation occurs predominantly near the jet centerline. For 86 μm particles, the value is everywhere quite small as compared to the production peak. The peak extra dissipation is quite large for the 55 μm particles at this relatively heavy loading. For both particle classes, the extra dissipation is very small in the center of the shear

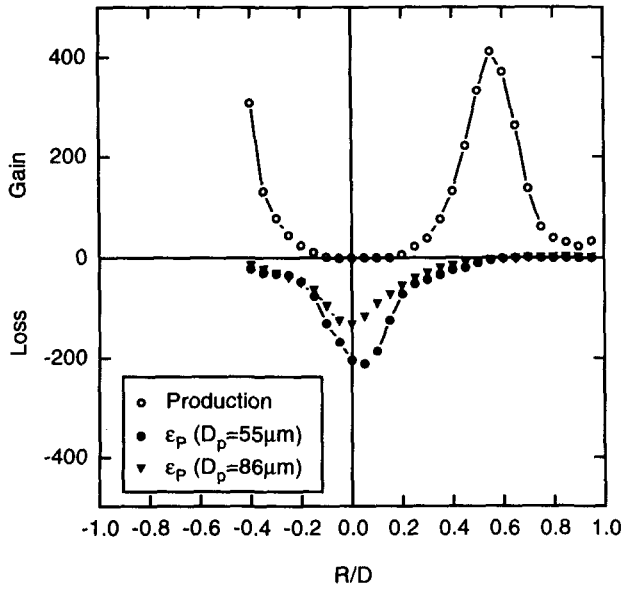

Figure 17. Extra dissipation of turbulent kinetic energy by particles for (a) 86 μm particles and (b) 55 μm particles.

layer where the production is strong. This coincides with the previous visualization studies that showed little change in the vortex ring structures even at high loading.

It is interesting to note that the extra dissipation is considerably larger for the 55 μm particles. Looking back at [2], we see that the particle time constant appears in the denominator of the force term and the fluid/particle velocity difference appears in the numerator. Both sizes of particles have a relatively large Stokes number, so neither size particle can follow the flow fluctuations well. Therefore, the velocity difference is controlled by the fluid velocity development. The force term is controlled by the particle time constant since the numerator is approximately the same for both size particles. This result cannot be extrapolated to much smaller particles. Particles with smaller time constants will follow the fluid velocity fluctuations better, and the quantity $(\overline{u_i u_i} - \overline{u_i v_i})$ will fall towards zero. Very small particles will follow the flow precisely and the extra dissipation term will be zero.

4. CONCLUSIONS

The present work demonstrates the difficulty of measuring the particle/fluid velocity correlation. Simultaneous measurements of the fluid and particle velocity are needed making the use of field techniques such as PIV mandatory. Light scattering from the large particles makes accurate measurement of the nearby fluid velocities difficult. Hassan *et al.* (1992) developed a semi-automatic technique to reduce this "halo" effect. However, even their technique still left a void in the fluid velocity measurement field near the particle. Noise in the individual measurements generally leads to a measured correlation value that is too low. The use of separate measurements of the fluid and particle velocities in a phase-locked flow eliminates these problems. However, the phase-locked technique results in correlation values which are too high because it neglects the effects of any non-phase-locked motions. Also, the requirement of phase-locking restricts the measurement technique to only a few very special flows.

Use of both simultaneous measurements (direct technique) and phase-locked measurements (indirect technique) have allowed us to bracket the range of the correlation and discover some interesting behavior in the particle-laden jet. The most surprising finding is that the correlation is higher for the larger particles. Generally we expect that the correlation will be a monotonically decreasing function of the particle time constant. The more inertia a particle has, the less able it is to follow the turbulent fluctuations. However, the present measurements have shown that we must also consider the mean motion of the different sized particles. Here, the 55 μm particles were accelerated rapidly from the jet exit and achieved a mean velocity substantially larger than the convection velocity of the large vortex rings. The 86 μm particles accelerated more slowly and perhaps coincidentally reached a velocity which was almost the same as the vortex ring convection velocity. Therefore, the turbulence field seen by the two particle classes was considerably different, and the larger particles were able to respond more faithfully to the fluid fluctuations. This same mean velocity effect produced particle clusters which were at much different phases relative to the vortex rings for the two sizes of particles.

The particle/fluid velocity correlations are of critical importance in modeling particle-laden flows. The results presented here show that the two-phase PIV technique can be used to provide reasonable estimates of the correlations with direct measurements of both phases simultaneously. This is important because there are only a few flows in which the dominant turbulence structure can be phase locked via acoustic or other forcing. Therefore, only the direct technique can be used in most turbulent flows. This technique now should be applied to measure the particle/fluid velocity correlation in a wider range of flows encompassing cases with fully three-dimensional turbulence structure.

The measurements of the extra dissipation of turbulence by particles neglected the azimuthal component of the velocity. This was expected to make a relatively small contribution to the extra dissipation for this flow. The extra dissipation was large near the jet centerline where the particles were clustered. This term was considerably larger for the 55 μm particles because of the smaller correlation between the fluid and particle velocities. It is important to note that the particle concentration fluctuations were highly correlated to the fluid velocity field. Neglect of the triple correlation terms in [2] (as was done to derive [3]) is not warranted in flows where the vortex

structure produces strong preferential concentration of the particles. Use of the extra dissipation term as shown in [1] is recommended for future work.

The peak value of the extra-dissipation term is less than half of the peak production. Recall, that this extra-dissipation was calculated for an assumed mass-loading ratio of unity. This is a relatively large mass loading within the dilute regime. The peak dissipation occurs on the jet centerline while the peak production occurs in the center of the jet shear layer. One would thus expect the extra dissipation to have a relatively minor effect on the growth of the shear layer turbulence levels.

Acknowledgements—The authors are grateful for the support of the National Science Foundation through Grant Number CTS-9312496. This collaboration was originally suggested by Professors K. Hishida and M. Maeda of Keio University who also loaned some of the important equipment.

REFERENCES

Beckel, D. L., Ainley, S. B., Thompson, J., Rogers, C. B. & Eaton, J. K. 1995 Measurements in the particle–Lagrangian reference frame. *6th Intl Symposium on Gas–Solids Flows*, Hilton Head, SC.

Eaton, J. K. & Fessler, J. R. 1994 Preferential concentration of particles by turbulence. *Int. J. Multiphase Flow* **20 Suppl.**, 169–210.

Hassan, Y. A., Blanchat, T. K., Seely, C. H. Jr & Canaan, R. E. 1992 Simultaneous velocity measurements of both components of a two-phase flow using particle image velocimetry. *Int. J. Multiphase Flow* **18,** 371–395.

Kiger, K. T. & Lasheras, J. C. 1995 The effect of vortex pairing on particle dispersion and kinematic energy transfer in a two-phase turbulent shear layer. *J. Fluid Mech.* **302,** 149–178.

Kulick, J. D., Fessler, J. R. & Eaton, J. K. 1994 Particle response and turbulence modification in fully developed channel flow. *J. Fluid Mech.* **277,** 109–134.

Longmire, E. K. & Eaton, J. K. 1992 Structure of a particle-laden round jet. *J. Fluid Mech.* **236,** 217–257.

Sakakibara, J., Hishida, K. & Maeda, M. 1993 Measurements of thermally stratified pipe flow using image processing techniques. *Experiments in Fluids* **16,** 82–96.

Wicker, R. B. & Eaton, J. K. 1994a Near field of a coaxial jet with and without axial excitation. *AIAA J.* **32,** 542–546.

Wicker, R. B. & Eaton, J. K. 1994b Structure and control of particle-laden coaxial jet with and without annular swirl, Mech. Engrg Dept. Rept. MD-68, Stanford University.